DOCTORATE OF PHILOSOPHY

Schrödinger's Catwalk

BRIAN FLYNN

UNIVERSITY OF BRISTOL

December, 2020

CONTENTS

LIST OF TABLES

LIST OF FIGURES

LISTINGS

ACRONYMS

AIC   Akaike information criterion. 84, 86
AICC   Akaike information criterion corrected. 84

BF   Bayes factor. 25–27, 33, 35, 48, 51, 55, 57, 61, 63, 64, 80, 81, 87, 89–91, 93–95
BFEER Bayes factor enhanced Elo ratings. 80, 81, 93, 94, 96
BIC   Bayesian information criterion. 86

CLE   classical likelihood estimation. 13

EDH   experiment design heuristic. 18–23, 26, 35, 45, 55, 56, 83
ES   exploration strategy. 27–31, 33–35, 40, 43, 45, 49, 51, 61, 65, 67, 75, 79, 105, 108
ET   exploration tree. 28, 29, 31, 33–35, 45, 47, 75

FH   Fermi-Hubbard. 58
FP   false negatives. 78
FP   false positives. 78

GA   genetic algorithm. iii, 34, 67, 71, 74, 75, 80, 82, 83, 88, 90, 93, 96–98
GES   genetic exploration strategy. 67, 78, 93, 94, 97

HPD   high particle density. 18

IQLE   interactive quantum likelihood estimation. 13, 14, 93, 94

LTL   log total likelihood. 16

ML   machine learning. 6, 26, 27, 78
MS   model search. 27–29, 31, 35, 43, 45
MVEE minimum volume enclosing ellipsoid. 18

NV   nitrogen-vacancy. 9
NVC   nitrogen-vacancy centre. 14

OF   objective function. iii, 67, 68, 74, 75, 78, 80, 81, 83,
          84, 88, 91–93

PGH   particle guess heuristic. 19, 20, 45

QHL   quantum Hamiltonian learning. 8–14, 16, 18, 20–22,
          25–27, 31–35, 40, 43, 48, 55, 56, 75, 93, 94, 105
QL   quadratic loss. 17
QLE   quantum likelihood estimation. 13, 32
QMLA   Quantum Model Learning Agent. ii, iii, vii, 8, 13,
          24, 25, 27–31, 34, 35, 40, 43–49, 51, 52, 60, 61, 63–65,
          67, 72, 74–77, 83, 87, 88, 90, 91, 93, 94, 96–98, 105

SMC   sequential monte carlo. 11–13, 15, 18, 19, 22, 31

TLTL   total log total likelihood. 16, 25–27, 35, 84, 91
TN   true negatives. 78
TP   true positives. 78

GLOSSARY

term   Individual constituent of a model, e.g. a single
                                operator within a sum of operators, which in total
                                describe a Hamiltonian. . 24

volume   Volume of a parameter distribution's credible re-
                                gion.. 18, 55, 56, 63

win rate   . 48, 49

Part I

EXPERIMENTAL STUDIES

NITROGEN VACANCY CENTRE

It is of primary interest to apply the QMLA algorithm to real-life, experimental systems. In this chapter we devise an exploration strategy (ES) to operate in conjunction with experimental data in order to characterise an electron spin in an nitrogen-vacancy (NV) centre in diamond. In particular, we model, through Hamiltonian terms, interactions between the spin and the spin bath in which it resides, so that QMLA is finding an effective model for the open system dynamics.

Here we will first introduce a basic picture of NVCs, using basic but nonstandard nomenclature for simplicity; for thorough descriptions of the underlying physics, readers are referred to [1]. We next discuss the target system with respect to its modelling, determining the suitable terms which *might* represent the NVC's interactions, to inform the starting point for the QMLA. Finally we describe the implementation of an ES for the examination of the NVC, and the results of the QMLA procedure.

1.1 NITROGEN-VACANCY CENTRE

NV centers are point defects in diamond, occuring naturally [2] or synthetically [3, 4]. A substitutional nitrogen-14 (^{14}N) isotope is embedded in a lattice of carbon atoms in diamond, adjacent to a lattice vacancy, such that it is surrounded by three carbon-13s (^{13}Cs) [5]. Of the ^{14}N atom's five valence electrons, three bond with nearby ^{13}Cs; the remaining two unbonded electrons for a lone pair and can be thought of as a single spin-$\frac{1}{2}$ particle. The adjacent lattice vacancy has three unbonded electrons, two of which bond together leaving a single unpaired electron. The single electron in the lattice vacancy, together with the effective lone pair of the ^{14}N, form a a system of two spin-$\frac{1}{2}$ particles. Such systems have been thoroughly studied; of particular interest are the resultant *triplet* states, i.e. the allowed permutations of the two particles with total quantum spin $S = 1$, with magnetic spin multiplicity allowing $m_s = -1, 0, 1$, giving rise to three distinct energy levels for the system.

A *manifold* is a set of states differing only slightly, for example states near the absolute ground state manifold might differ only in magnetic spin quantum number, and can be characterised as the ground state manifold. We consider two principle manifolds of the system: the ground state and excited manifolds, each consisting of three states, corresponding to the allowed values for magnetic spin m_s, see Fig. 1.1a. For brevity, we denote states with reference to their magnetic spin and manifold, e.g. the state in the ground state manifold with $m_s = 0$ is denoted $|m_s = 0\rangle_g$. In the absence of a magnetic field, the states corresponding to $|m_s = \pm 1\rangle$ are degenerate, but in the presence of a magnetic field, B, they have distinct energy levels, referred to as the Zeeman effect, Fig. 1.1b.
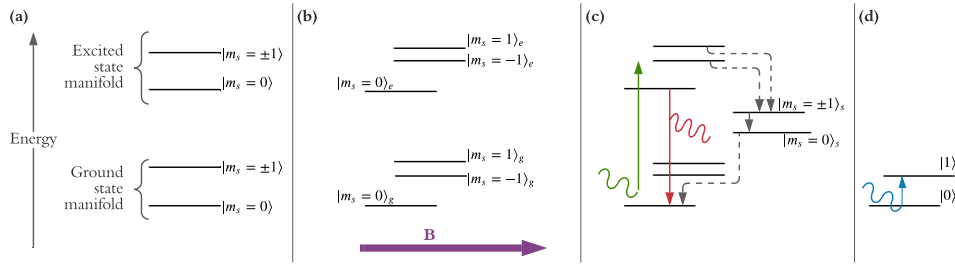
Figure 1.1: Simplified depiction of energy levels of the nitrogen-vacancy centre, corresponding to its triplet state. **a**, With no external field, the system simply has excited and ground-state manifolds, each of which consist of two energy levels depending on the magnetic spin, m_s. **b**, In the presence of a magnetic field (purple, B), the magnetic spins have distinct energy levels, i.e. Zeeman splitting. States are denoted by their magnetic spin and subscripted by their manifold. **c**, Application of a green (532nm) laser excites the NVC from any of the states in the ground state manifold to the excited manifold. The dominant decay mechanism for the excited states are shown: (i) $|m_s = 0\rangle_e \rightarrow |m_s = 0\rangle_g$ (red line) through the emission of a red (637nm) photon; (ii) $|m_s = \pm 1\rangle_e \rightarrow |m_s = 0\rangle_g$ (dotted grey lines) via the shelving manifold which allows for non-spin-preserving transition, and does not emit a photon. **d**, Computational basis states $|0\rangle$ and $|1\rangle$ are assigned to the two lowest energy states. The difference in energy between these states is such that a microwave (MW, blue) photon can trigger transition from $|0\rangle$ to $|1\rangle$, as well as states in between such as $|+\rangle$, allowing for the implementation of quantum logic gates.

We designate the state $|m_s = 0\rangle_g$ as the basis state $|0\rangle = \begin{pmatrix} 1 \\ 0 \end{pmatrix}$, and $|m_s = -1\rangle_g$ as $|1\rangle = \begin{pmatrix} 0 \\ 1 \end{pmatrix}$, such that we have defined a qubit and computational basis, Fig. 1.1d. By shining a laser of 532nm (green) on the NVC, it is excited to the excited manifold, from which it decays back to the ground state manifold. Importantly, the process of this decay can be exploited for the preparation of the NVC in the computational basis state $|0\rangle$. That is, the dominant decay process from $|m_s = 0\rangle_e$ is spin-preserving, so it ends in $|m_s = 0\rangle_g$. On the other hand, had the NVC been in the $|m_s = \pm 1\rangle_e$, the dominant decay process is through a shelving (singlet) state, and does not preserve spin, such that it also decays to the $|m_s = 0\rangle_g$. Therefore, irrespective of the initial state, by shining the green laser on the NVC, it is most likely that it has been prepared in $|m_s = 0\rangle_g = |0\rangle$, providing us a starting point from which to perform computation.

The difference in energy between $|0\rangle$ and $|1\rangle$ is addressible optically: by shining a pulse at the NVC, we can oscillate the qubit between the two levels. Likewise, having initialised the state to $|0\rangle$, we can perform a $\pi/2$ rotation about the logical z-axis, by running the laser for half the time, resulting in the state $|+\rangle$. We can similarly devise radiation to achieve quantum gates and operations on our NVC qubit. We depict these cycles in Fig. 1.1c.

We can further exploit the decay mechanism to compose a readout procedure, to infer the population of $\{|0\rangle, |1\rangle\}$ at a given instant, for example following the application of gates to the system. We know that the excitation due to the green laser is spin-preserving, i.e. when the NVC has been excited to $|m_s = 0\rangle_e$, it had originated in $|m_s = 0\rangle_g$. We also know that the decay $|m_s = 0\rangle_e \rightarrow |m_s = 0\rangle_g$ is spin preserving, with the emission of a red photon: by simply counting the number of photons emitted, we quantify the population of $|0\rangle$ at the time of query. On the contrary, when the $|m_s = -1\rangle_g$ is excited, spin is also preserved, so it goes to $|m_s = -1\rangle_e$; but $|m_s = -1\rangle_e$ decays through the shelving state as outlined earlier, *without* the emission of a photon. We can hence infer the population of $|m_s = -1\rangle_g$ at the time of query by the fraction of incidents which don't emit a photon. That is, say we first calibrate the system by retaining the green laser for some time: after a few μs, a steady state is achieved where the majority of the time, the triplet is in the state $|0\rangle = |m_s = 0\rangle_g$. Then, excitation from the same laser results in the excitation to $|m_s = 0\rangle_e$, which decays back to $|m_s = 0\rangle_g$ and emits a photon in the process; by counting the red photons emitted in a certain time window – equivalently, measuring the photoluminescence (PL) signal – we benchmark the population of $|0\rangle$ when nothing else has happened as p_0. Now, when we apply gates (i.e. pulses) to the NVC, we can similarly read out the population of $|0\rangle$ as p'_0, and infer that the likelihood that the is found in the initial state $|0\rangle$ is p'_0/p_0. We can use this quantity as the likelihood within quantum likelihood estimation (QLE), allowing us to learn from the NVC, as we will discuss in the next sections.

In summary then, by assigning basis states $|0\rangle, |1\rangle$ to energy levels of the ground state manifold, we are able to ensure the preparation of the NVC in $|0\rangle$ by first shining a green laser on the NVC. We can then apply radiation to achieve quantum logical gates on the system, and read out the final state of the system, again by shining a green laser and observing the emitted photons (PL) and inferring the population level of each basis state. We represent these concepts in a simplified format in Fig. 1.1.

1.2 TARGET SYSTEM

We take the axis of the NVC, i.e. the axis connecting the ^{14}N with the lattice vacancy, as the z-axis. There are clearly a huge number of interactions to which the NVC is subject: we choose to focus on its interactions with the environment, i.e. with nuceli in the same diamond, which dictate its decoherence. These interactions are characterised by hyperfine terms [6]. The overall Hamiltonian for such systems, where the set of nuclear sites is $\{\chi\}$, is given by

$$\hat{H}_{\text{full}} = \Delta_{\text{gs}}\hat{S}_z^2 + \mu_B g\mathbf{B} \cdot \mathbf{S} + \mathbf{S} \cdot \sum_\chi \left(\mathbf{A}_\chi \cdot \hat{I}_\chi\right) + P\hat{I}_z^2 + \mu_n g\mathbf{B} \cdot \sum_\chi \hat{I}_\chi. \tag{1.1}$$

We will describe each term, as well as approximations which enable us to simplify the space considerably.

- Isolated-spin terms, i.e. describing the spin independent of the environmental nuclei

- $\Delta_{\text{gs}} \hat{S}_z^2$: the *zero-field* splitting, i.e. without any external (magnetic) field, the spin oscillates rapidly, with $\Delta_{\text{gs}} \sim$ GHz.
  - $\mu_B g \mathbf{B} \cdot \mathbf{S}$: the spin's precession about the magnetic field, $\mathbf{B} = \begin{pmatrix} B_x & B_y & B_z \end{pmatrix}$, via the total spin operator[1] $\mathbf{S} = \begin{pmatrix} \hat{S}_x & \hat{S}_y & \hat{S}_z \end{pmatrix}$, where μ_B is the Bohr magneton and g is the g-factor (≈ 2, simplified from the g-factor tensor).
- Hyperfine terms
  - $\hat{S} \cdot \sum_\chi \left(\mathbf{A}_\chi \cdot \hat{I}_\chi \right)$: The NVC total spin operator $\mathbf{S}$ couples with each site, χ. At each site there is a nucleus which has total spin operator $\mathbf{I}_\chi = \begin{pmatrix} \hat{I}_x & \hat{I}_y & \hat{I}_z \end{pmatrix}_\chi$. $\mathbf{A}$ is the hyperfine tensor, containing the hyperfine parameters of interest.
- Bath-only terms, i.e. describing the other nuceli independent of the spin
  - $P \hat{I}_z^2$: the quadrupole splitting, i.e. this term gives the splitting of the ^{14}N's hyperfine splitting, which does not meaningfully contribute to the short-decay processes in the experiments described in the next section.
  - $\mu_n g \mathbf{B} \cdot \sum_\chi \hat{I}_\chi$: μ_n is the nuclear magneton and g is again the g-factor.

Given that we are interested in the spin and its interactions with the environment only, we can immediately drop the bath-only terms, by assuming the bath is static apart from its interactions with the NVC. This is a usual assumption in the treatment of open system dynamics, to allow for focus on the dominant interactions for the system of interest [7]. Additionally, since the zero field splitting contributes a constant shift in energy, we can safely omit it by moving to the rotating frame. We are then left only with the second and third terms of Eq. (1.1).

1.2.1 *Mapping to model terms*

Next we will focus on mapping the remaining terms to operators to compose the set of terms $\mathcal{T}$ to use in our ES. In our modelling, the NVC spin is represented by the first logical qubit, with a further $|\{\chi\}|$ qubits, each representing a unique nuclear site, as discussed later in this section. As standard, we take the axis[2] of the NVC as parallel to the qubit's z-axis.

The first terms included come from the spin's precession about the magnetic field. It is usually assumed that the external, applied magnetic field is well-aligned with the spin qubit's z-axis; here we will treat this determination as the role of QMLA, i.e. we will endeavour to establish whether the x-, y-axis components of the magnetic field are important for describing the spin's dynamics. Then, we have

$$\mu_B g \mathbf{B} \cdot \mathbf{S} = \mu_B g \begin{pmatrix} B_x & B_y & B_z \end{pmatrix} \cdot \begin{pmatrix} \hat{S}_x & \hat{S}_y & \hat{S}_z \end{pmatrix} \rightarrow \alpha_x \hat{S}_x + \alpha_y \hat{S}_y + \alpha_z \hat{S}_z, \tag{1.2}$$

---

1 We invoke an inexact representation of high dimensional tensors here for ease of interpretation. For instance, the total nuclear spin operator exists in arbitrary dimension (depending on the number of sites modelled), but we present it simply as $\mathbf{I} = \begin{pmatrix} \hat{I}_x & \hat{I}_y & \hat{I}_z \end{pmatrix}$ at each site to convey that we can separate the terms in the construction of models.

2 The axis connecting the ^{14}N with the lattice vacancy.

with $\alpha_i = \mu_B g B_i$. The spin's rotation terms to be included in QMLA's deliberations are therefore

$$\mathcal{T}_s = \{\hat{S}_x, \hat{S}_y, \hat{S}_z\} \tag{1.3}$$

Next, let's focus on the hyperfine coupling term. In general we sum over the nuclear sites $\{\hat{H}_i\}$, since the spin will interact with every nucleus to some extent; We show in [8] that a realistic system requires modelling a finite-size bath of $|\{\chi\}| \sim 15$ nuclei to capture the dynamics of interest, which is infeasible for complete characterisation via classical simulation, where we are limited to ~ 11 qubit calculations[3]. Instead, by focusing only on the *short-time* dynamics of the NVC, we can isolate the effects of dominant interactions, most notably with a single nearby ^{13}C. Indeed, by assigning a first qubit as representing the NVC spin, we can map the entire environment onto a generic second *environmental qubit*, representing the amalgamation of said interactions, though we can think of the two-qubit system as the NVC coupled with a single ^{13}C [6].

$$\mathbf{S} \cdot \sum_{\chi} (\mathbf{A}_\chi \cdot \mathbf{I}_\chi) \rightarrow \mathbf{S} \cdot \mathbf{A} \cdot \mathbf{I} \tag{1.4}$$

This clearly reduces the dimension of our approximation, the number of qubits, n_q from $n_q = 1 + |\{\chi\}|$ to $n_q = 2$, since now we only retain qubits for the NVC and the ^{14}N (which also represents the entire bath). The hyperfine tensor $\mathbf{A}$ consists of the hyperfine parameters, i.e. the strength of correspdoning interactions.

$$\mathbf{A} = \begin{pmatrix} A_\perp & 0 & 0 \\ 0 & A_\perp & 0 \\ 0 & 0 & A_\parallel \end{pmatrix}, \tag{1.5}$$

where $A_\perp$ is the non-axial hyperfine coupling term and $A_\parallel$ is the axial coupling term, since the axis of the NVC is used to define the *z*-axis for our qubits.

The total spin operators – of the NVC operating on the first logical qubit and the environmental qubit on the second – can be thought of as

$$\begin{aligned} \mathbf{S} &= (\hat{S}_x^{(1)} \quad \hat{S}_y^{(1)} \quad \hat{S}_z^{(1)}) \\ \mathbf{I} &= (\hat{I}_x^{(2)} \quad \hat{I}_y^{(2)} \quad \hat{I}_z^{(2)}) \end{aligned} \tag{1.6}$$

So we can write,

$$\begin{aligned} \mathbf{S} \cdot \mathbf{A} \cdot \mathbf{I} = &A_\perp \hat{S}_x \hat{I}_x + A_\perp \hat{S}_y \hat{I}_y + A_\parallel \hat{S}_y \hat{I}_y \\ &+ A_{xy} \left(\hat{S}_x \hat{I}_y + \hat{S}_y \hat{I}_x\right) \\ &+ A_{xz} \left(\hat{S}_x \hat{I}_z + \hat{S}_z \hat{I}_x\right) \\ &+ A_{yz} \left(\hat{S}_y \hat{I}_z + \hat{S}_z \hat{I}_y\right) \end{aligned} \tag{1.7}$$

Off-diagonal terms, referred to hereafter as *transverse* terms ($\hat{S}_i \hat{I}_j$ where $i \neq j$), are usually neglected [9]; here we will emply QMLA to determine whether their contributions are worthy of inclusion, although we consider only $\{\hat{S}_x \hat{I}_y, \hat{S}_x \hat{I}_z, \hat{S}_y \hat{I}_z\}$ for brevity. In total then, the hyperfine terms to be entertained by QMLA are

$$
\mathcal{T}_{HF} = \begin{Bmatrix} \hat{S}_x \hat{I}_x, & \hat{S}_y \hat{I}_y, \hat{S}_z \hat{I}_z, \\ \hat{S}_x \hat{I}_y, & \hat{S}_x \hat{I}_z, \hat{S}_y \hat{I}_z \end{Bmatrix}. \tag{1.8}
$$

Finally, combining Eq. (1.3) and Eq. (1.8), we have the full set of terms to incorporate into QMLA ES:

$$
\mathcal{T}_{NV} = \begin{Bmatrix} \hat{S}_x, & \hat{S}_y, \hat{S}_z, \\ \hat{S}_x \hat{I}_x, & \hat{S}_y \hat{I}_y, \hat{S}_z \hat{I}_z, \\ \hat{S}_x \hat{I}_y, & \hat{S}_x \hat{I}_z, \hat{S}_y \hat{I}_z \end{Bmatrix}. \tag{1.9}
$$

We introduce a shorthand notation to ease model representation for the remainder of this chapter. Recall that we have defined a two-qubit Hilbert space for model construction. Terms which affect only the spin act only on the first qubit, $\hat{S}_i = \hat{\sigma}_i \otimes \hat{\mathbb{1}}$, where $\hat{\sigma}_i$ is the Pauli operator giving rotation about the *i*-axis, and $\hat{\mathbb{1}}$ is the one-qubit identity matrix. Retaining the hyperfine notation, for the expectedly-dominant diagonal terms, we denote $\hat{A}_i = \hat{S}_i \hat{I}_i = \hat{\sigma}_i \otimes \hat{\sigma}_i$. We refer to the less-dominant off-diagonal terms as *transverse* terms, $\hat{T}_{kl} = \hat{S}_k \hat{I}_l = \hat{\sigma}_k \otimes \hat{\sigma}_l$. We can hence rewrite Eq. (1.9) as

$$
\mathcal{T}_{NV} = \begin{Bmatrix} \hat{S}_x, & \hat{S}_y, \hat{S}_z, \\ \hat{A}_x, & \hat{A}_y, \hat{A}_z, \\ \hat{T}_{xy}, & \hat{T}_{xz}, \hat{T}_{yz} \end{Bmatrix}. \tag{1.10}
$$

We also use a succinct representation for brevity, e.g. $\hat{S}_{xy} \hat{A}_z = \hat{S}_x + \hat{S}_y + \hat{A}_z$, where parameters $\alpha_x, \alpha_y, \alpha_z$ are implicitly assumed.

1.2.2 *Prior knowledge*

The spin-only terms, $\hat{S}_i$, are consequences of the magnetic field, which is usually assumed as aligned with *z*-axis, such the *x*-, *y*-axis compoenents are negligible; $\hat{S}_z$ is expected in the range $\sim 2 - 3$MHz. Likewise, the hyperfine terms, $\hat{A}_i$ are expected in the range of $\sim$ MHz [10], while in the *secular approximation* only the *z*-component is expected to contribute substantially [11]. The non axial hyperfine terms, i.e. the transverse terms $\hat{T}_{kl}$ are not usually included in effective models, but can be found of order $\sim \mathcal{O}(10\text{kHz})$ [12]. We utilise this prior understanding of the system to inform the parameter range used for training candidate models: for each of the terms

---

3 This limitation arises from the requirement to compute the total evolution of the global state, involving calculation of $e^{-i\hat{H}t}$, i.e. the characterisation of an n_q-qubit model depends on classical exponentiation of the $2n_q \times 2n_q$ Hamiltonian for each particle and experiment in classical likelihood estimation (CLE), which is a prohibitive expense.
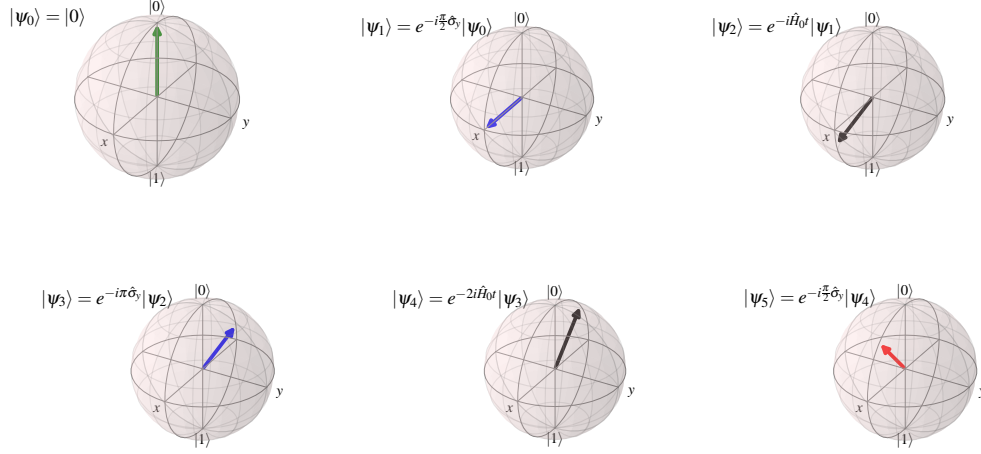
Figure 1.2: States of spin qubit at each stage of Hahn echo sequence.
The state of the NVC spin is initialised by a green laser into state $|\psi_0\rangle = |0\rangle$. We then apply a rotation about the y-axis (i.e. a pulse), yielding the state $|\psi_1\rangle = |+\rangle$. The system is then allowed to evolve according to its own $\hat{H}_0$ for t, $|\psi_2\rangle = e^{-i\hat{H}_0 t}|+\rangle$. We apply a second pulse, this time for a π-rotation about the y-axis, $|\psi_3\rangle = e^{-i\pi\hat{\sigma}_y}e^{-i\hat{H}_0 t}|+\rangle$. Again the system evolves according to interactions with the environment, this time for $t' = 2t$. We apply a final pulse to rotate about the y-axis again, effectively either returning the spin to near the $|0\rangle$ axis, or near the $|1\rangle$ axis. Here $|\psi_5\rangle$ is roughly half way between $|0\rangle$ and $|+\rangle$, i.e. along the z-axis. The spin is read out from $|\psi_5\rangle$ via the NVC's photoluminescence. Here $\hat{H}_0 = 0.25\,\hat{\sigma}_y$ was evolved for $t = 0.5$ (arbitrary units), and the final state overlap with the initial state, i.e. the likelihood of measuring the spin in $|0\rangle$ is $\Pr(0|\hat{H}_0, t) = 0.865$.

in Eq. (2.3), we will adopt a normal prior distribution of 4 ± 1.5MHz. This is sufficiently specific to ensure the training subroutine operates in a physically meaningful – and likely appropriate – space, whlie also broad enough to allow for significant differences between expectation and reality, as well as supporting hypotheses where each parameter is zero, such that such negligible contributions can be identified.

1.2.3 *Experimental procedure*

We have decided to characterise the hyperfine interactions of the NVC; these are evident most strongly at very short timescales [13]. To isolate the effects of the hyperfine interactions, we run Hahn echo experiments, which are known to emphasise weak interactions. Hahn echo sequences attempt to decouple the spin's dynamics from the nuclear bath [14, 9, 13, 15, 16] providing a helpful platform for studying residual contributions of terms in Eq. (2.3). The NVC
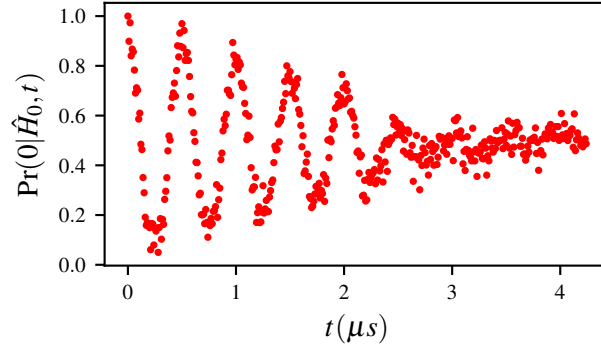
Figure 1.3: Raw data for the nitrogen-vacancy centre's dynamics. The *y*-axis shows the photoluminescence of the NVC, equivalently the likelihood $\Pr(0|\hat{H}_0, t)$.

qubit undergoes a series of evolutions – either according to application of quantum logic gates or the natural evolution of the system interacting with its environmen We depict the stages of the experiment in Fig. 1.2, starting from the initialised $|0\rangle$ through to its final state which is read out through PL, both of which as described in Section 1.1.

In particular, the final state, $|\psi\rangle_5$, is read out, effectively by projection onto $|0\rangle$; we can interpret the PL after evolution time t as the likelihood that the NVC is found in $|0\rangle$ after evolution of its *true* Hamiltonian, $\hat{H}_0$. That is, we assign this projection as the quantity $\Pr(0|\hat{H}_0, t)$ (the likelihood), and it can be used within likelihood estimation in order to refine a candidate model $\hat{H}_j$, effectively[4] by changing the structure of $\hat{H}_j$ until $\Pr(0|\hat{H}_0, t) \approx \Pr(0|\hat{H}_j, t) \ \forall t$.

By varying the evolution time of the Hahn-echo sequence, we can map the likelihood against time, which we can view as capturing the dynamics of the NVC spin **??**. We vary time up to $t \sim 4\mu s$ in the short-time range in intervals of $\Delta t = 50ns$, so we have 425 data points. Importantly, the data for the studied NVC is taken once and analysed offline, i.e. QMLA does not have complete authority to design experiments to run on the NVC, although it can aim to choose the most informative t available in the predefined set; we will discuss the consequences of this restriction later in this chapter.

1.3 EXPLORATION STRATEGY

Finally, then, we are in a position to describe the specific implementation details which allow QMLA to study this NVC system. Recalling the terminology of QMLA from **??**, we design an exploration strategy (ES) specifically for the system under study. The ES will account for the details listed in this chapter so far, in summary:

- we attempt to assign a model, $\hat{H}'$, to the NVC;

---

4 Of course this is a gross simplification of quantum Hamiltonian learning (QHL) which is described fully in **??**
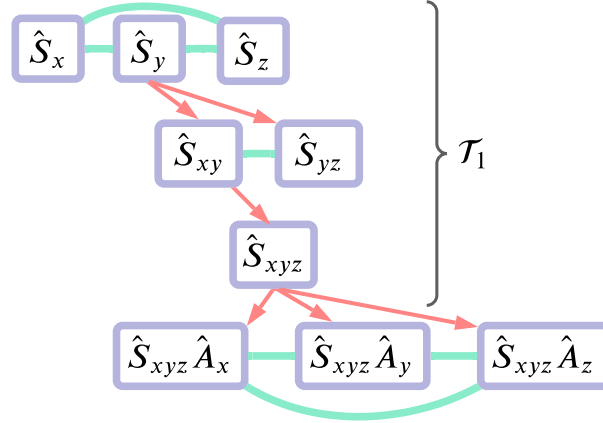
Figure 1.4: Greedy model search. Models (purple) are placed on branches, trained and consolidated (green) as in **??**, with the branch champion spawning (red) candidates to place on the subsequent branch. Branches are grouped in tiers, correspdoning to levels of approximation: the first tier of the model generation strategy is shown, where $\mathcal{T}_1 = \{\hat{S}_x, \hat{S}_y, \hat{S}_z\}$ is explored. The final champion from the first tier seeds the second tier.

- – we especially focus on its hyperfine interactions;
- in particular, we use a 2-qubit approximation;
  - – the first qubit represent the spin itself;
  - – the second qubit represents the environment in which the NVC resides;
- we query the NVC by performing Hahn echo experiments (Fig. 1.2);
- the outcome of those experiments are thought of as the system's likelihoods (Fig. 1.3);
- likelihoods are used for the training of individual candidate models;
- candidate models are composed of the terms defined in Eq. (2.3).

As outlined in **??**, the central role of any ES is to specify the model generation procedure, which QMLA relies upon for deciding the next set of candidate models to test. In this case, we exploit some intuition and prior knowledge of how such systems work, to design a bespoke model generation subroutine: we can think of this as a midway point between the completely specified ESs used for identifying the underlying lattices from a prescribed set in **??**, and the entirely general genetic algorithm which does not restrict model generation, of **??**. We use the standart structure of exploration trees (ETs) introduced in **??**, where models are placed on consecutive branches, μ, with branches consolidated by complete pairwise comparisons, mediated through Bayes factors (BFs), resulting in the selection of a single branch champion, $\hat{H}_{C(\mu)}$.

We use a *greedy search rule*: terms are added one-by-one to gradually increase the complexity of candidate models until terms are exhausted [17]. We break the ET into three distinct tiers, each corresponding to an intuitive degree of complexity: the first tier involves the spin-only terms, $\mathcal{T}_1 = \{\hat{S}_i\}$; the second considers the hyperfine terms, $\mathcal{T}_2 = \{\hat{A}_i\}$; the final tier the transverse terms, $\mathcal{T}_3 = \{\hat{T}_i\}$. Within each tier, terms are added greedily to the previous branch's champion, $\hat{H}_{C(\mu)}$. So, the first branch is given by $\mu = \{\hat{S}_x, \hat{S}_y, \hat{S}_z\}$; say $\hat{H}_{C(\mu)} = \hat{S}_y$, then $\mu + 1$ determines that $\hat{S}_x, \hat{S}_z$ are not yet considerd, so it constructs the models $\hat{S}_{x,y}, \hat{S}_{y,z}$, e.g. Fig. 1.4. After exhausting all tiers, we consolidate the set of branch champions, $\mathbb{H}_C = \{\hat{H}_{C(\mu)}\}$, to determine the best model considered globally, $\hat{H}'$.

Clearly, this growth rule is partially deterministic, insofar as some models are gauranteed to be considered, while others are not reachable; indeed, the space of available models are heavily constrained, in particular models in later tiers will always involve all of the tier 1 models, e.g. $\hat{S}_x \hat{A}_y$ does not occur naturally. We account for this shortcoming with a final redcibility test, triggered if any of the parameters of $\hat{H}'$ are potentially negligible, i.e. are within one standard deviation of 0. This test simply removes such low-parmeter terms from $\hat{H}'$, giving a reduced global champion, $\hat{H}'_r$, and computes the BF between $\hat{H}', \hat{H}'_r$: if the BF indicates strong evidence in favour of the reduced version, we replace the champion model, $\hat{H}' \leftarrow \hat{H}'_r$. In effect, we thus verify the statistical significance of each term included in $\hat{H}'$.

The total model in Eq. (1.1) supports $N_t = 1 + 3 + 6|\chi| + 3 + 3|\chi| = 7 + 9|\chi|$ terms, which we reduced to a space of $N_t = 3 + 6|\chi| = 9$ through several approximations; even so, the remainng 2^9 permitted models were reduced further by building the logic of this ES from our intuition aroud existing knowledge of typical NVC systems, such the ES will only ever consider < 20 models per instance. The described ES seems overly perscriptive, but should be viewed as a first attempt at a generalisable approach: essentially we can view the tiers of the greedy search as characterising the system at various approximations, e.g. the first tier examines one-qubit terms, while subsequent tiers inspect 2-qubit terms. We can envision future work where the greedy search is gradually extended to less rigid approximations, enabling study of more complex quantum systems. This leads to some important remarks:

1. Realistic, near-term applications of QMLA can not be thought of as a solution to black-box characterisation problems: it must be used in conjunction with domain expertise for the system under study.

2. While this test-case yields promising results, the outcome of QMLA here may not be especially insightful, since the available model terms were so deliberately constrained – we demonstrate a use-case in Chapter 2 where a broader scope is enabled in simulation.

A common charge against QMLA supposes to first write down the most complex model, train it fully, and then infer which terms are negligible, in a similar process to the champion reduction test outlined here. While this may be feasible in the case described here, with $N_t = 9$ and a closed term set, this would scale poorly: adding just a second nuclear site increases the model search to a space of $N_t = 15$. Models of higher cardinality ($|\vec{\alpha}|$) demand higher N_e, N_p to train well, so immediately trainng the most involved model would require infeasible resources[5], and

risks significantly overfitting the data. It seems more appropriate to work "from the ground up", testing terms and keeping them only when justified, instead of training all terms and attempting to decouple their effects post-hoc.

1.3.1 *Test in simulation*

Before considering the real experimental data (Fig. 1.3), we first test the ES in simulation under ideal conditions. That is, we assume the ability to prepare arbitrary probe states, and use a random probe set (see **??**), and use the full expectation value as the likelihood, $|\langle\psi|e^{-i\hat{H}_j t}|\psi\rangle|^2$. Of course, this is infeasible since we presume access to the full state at the time of measurement, but this can be seen as a best-case scenario for this application, because the realistic case loses information by tracing out the environmental qubit at measurement. We vary the target $\hat{H}_0$, among a series of ten models, which are all valid models achievable by the ES.

Varying $\hat{H}_0$, allowing arbitrary probe preparation and particle guess heuristic (PGH) experiment design heuristic (EDH), i.e. case (i) from [8].

1.4 EXPERIMENT DESIGN CONSTRAINTS

Moving to analyse the experimental setup, there are a number of constraints which we must account for in training models. Firstly, the $\pi/2$-pulse applied to the prepared qubit ($|\psi_0\rangle \rightarrow |\psi_1\rangle$ in Fig. 1.2) means that the state before evolution is always $|+\rangle$ in the computational basis; this is a severe limitation on model training, as we saw in **??**. Moreover, this puts a bias on the interactions QMLA is likely to identify: we show in Fig. 1.2 how QHL performs in training the same model using (i) the probe set available experimentally; (ii) a more general (random) probe set. This has a noteworthy impact on the outcome of this study, since this suppression of terms means we are more likely to find some interactions than others, so we must add this caveat to the champion model.

The experiment was run until the NVC was deemed to have decohered, so Fig. 1.3 ceases at $t_{max} \sim 4\mu s$. As discussed in **??**, usually it is helpful to allow a experiment design heuristic (EDH) to choose the experimental controls, including the evoltuion time, t, against which the model is trained at each experiment; the default particle guess heuristic (PGH) attempts to select t at the upper boundary of times where the model is expected to be predictive, such as to maximise the information gained by the experiment (see **??**). Here, however, we can not allow the EDH to select arbitrary t, since we do not have data beyond t_{max}.

Clearly, we require a custom EDH to account for the constraints outlined, with the following considerations:

---

5 Note: in the case studies presented in this thesis, it was found that the same resources were sufficient for the simplest and most complex models, due to the relatively small number of terms therein. We expect for larger models, e.g. $|\vec{\alpha}| > 10$, that the resources allocated ought to be proportional to the cardinality, which is an in-built option in the QMLA software.

1. We may only assume access to the probe $|+\rangle$ on the spin qubit

   (a) we further assume the environmental spin is polarised by the same microwave pulse, such that the global probe available is $|\psi\rangle = |+\rangle |+'\rangle$, with $|+'\rangle = \frac{|0\rangle + e^{i\phi}|1\rangle}{\sqrt{2}}$ and ϕ is random [18].

2. We can not allow the choice of any t

   (a) Any $t > t_{\max}$, arising from a thin parameter distribution, must be mapped to some $0 < t \leq t_{\max}$.

   (b) All nominated t must be mapped to the nearest available t in the dataset so that the likelihoods are as close as possible to simulating the true system.

3. Much of the physics of interest occurs at relatively high times, i.e. because the rotation (MHz) terms dominate, the decay of the peaks can be seen as evidence of the bath, notably through hyperfine terms in the model.

   (a) We therefore wish to enforce that all models are trained on those data ($t \geq 2\mu s$), even if their parameter distribution is insufficiently narrow to yield those times naturally.

Accounting for these, we construct an EDH which mixes the robust, adaptive nature of PGH, useful for refining an initially broad $\Pr(\vec{\alpha})$, with a primitive, linear time-selection, useful to ensure the trained parameters at least attempt to account for the physics we are actually interested in. That is, with each model trained for N_e experiments, we train according to the standard PGH for the first $N_e/2$, but force the training to mediate over the available data for the latter $N_e/2$.

1.5 RESULTS

We apply the ES described in Section 1.3 to the raw data of Fig. 1.3; the results are summarised in Fig. 1.5.

We first focus on the overall outcomes: the most blunt figure of merit of interest is simply whether QMLA overfits or underits the true parameterisation. In preliminary analysis we run 500 instances with varying $\hat{H}_0$, and where the cardinality of $\hat{H}_0$ ranges, so we can broadly gauge the tendency towards over- and under-fitting: we see that in $\sim 50\%$ of instances the correct cardinality is found, rising to $\sim 86\%$ by allowing one fewer (additional) terms, Fig. 1.5**(b)**. Moreover, the champion models' are highly predictive: the median coefficient of determination between the systems' and corresponding champion models' data is $R^2 = 0.84$.

Then, considering the performance of the algorithm on whole, we perform runs of 100 instances on the exerpimental data as well as simulated data, where the simulation assumes[6] $\hat{H}_0 = \hat{S}_{xyz}\hat{A}_z$, The set of models selected most frequently are shown in Fig. 1.5**(c)**, and each model is trained with $N_e = 1000, N_p = 3000$, with the volumes of those models (in
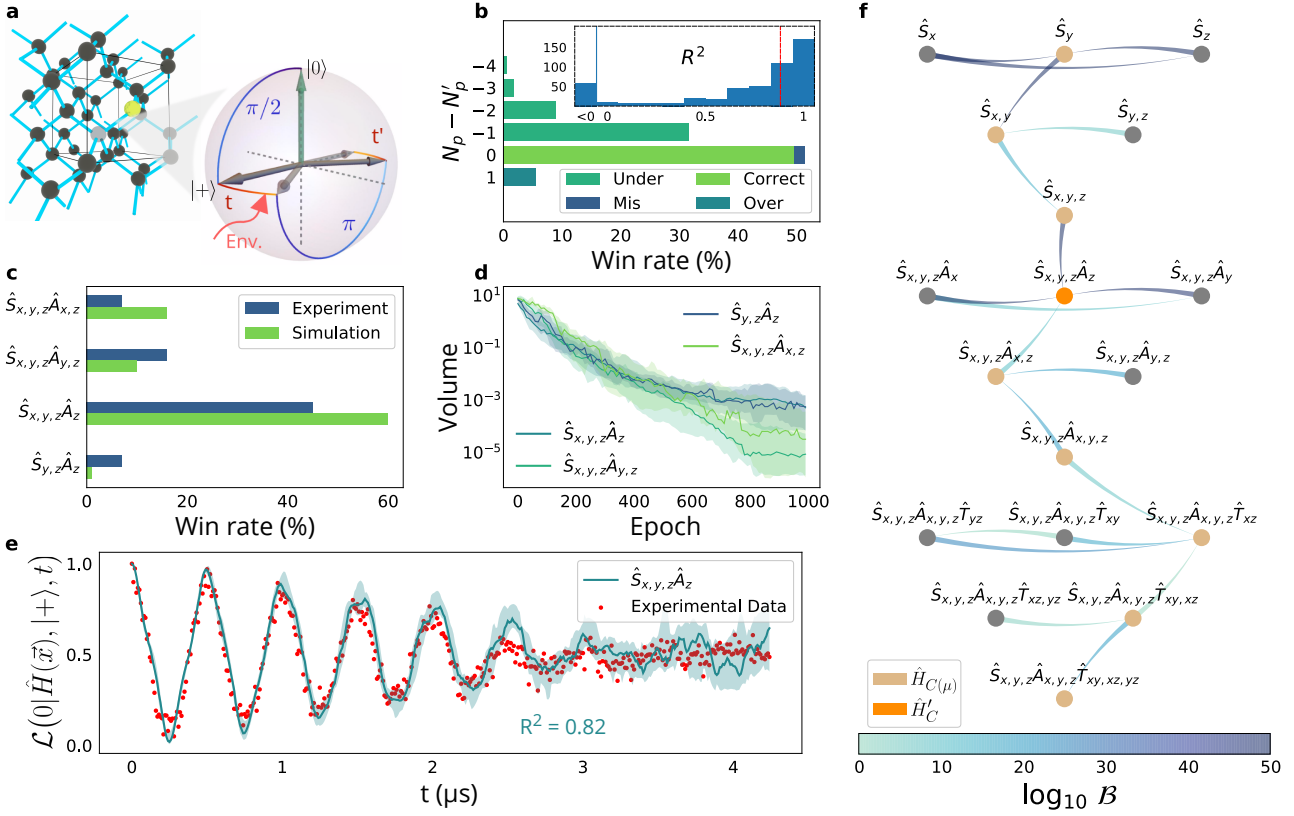
Figure 1.5: **a**, The carbon lattice providing the outer environment for the NV centre, along with the time evolution of the electron spin state (represented on a Bloch sphere) during the pulses for the Hahn-echo sequences. The final $\pi/2$ pulse is omitted. **b**, Simulation of 500 independent QMLA instances, where $\hat{H}_0$ is chosen randomly. The win rate is reported against the difference ($N_p - N_p'$) between the number of parameters in $\hat{H}'$ and $\hat{H}_0$, respectively. The *under-parameterised (over-parameterised)* class refers to models with less (more) parameters than $\hat{H}_0$. *Correct* indicates that exactly $\hat{H}_0$ was found. The *mis-parameterised* class groups models with the same parametrisation cardinality as $\hat{H}_0$, but different Hamiltonian terms. **Inset**, Histogram of occurrences of R^2 values for each retrieved $\hat{H}'$ against a sampling of datapoints from $\hat{H}_0$, with median $R^2 = 0.84$ (red dotted line). **c**, Win rates of top four models for 100 QMLA instances, against both simulated and experimental data. Simulations use $\hat{H}_0 = \hat{S}_{x,y,z}\hat{A}_z$. **d**, Total volume spanned by the parameters' prior across epochs, for the models in **c**. Shaded areas indicate 66% credible regions. **e**, Simulated likelihoods reproduced by the model with the highest win rate ($\hat{S}_{x,y,z}\hat{A}_z$, turquoise), compared with corresponding NV-centre system experimental data (red-dots, extracted from the observed PL of the first Hahn-echo decay). Error bars smaller than the dots (see Methods). **f**, A single QMLA instance against experimental data in **e**, depicted as a . The thin end of each edge points to the favoured model; the colour of the edges maps $\log_{10}\mathcal{B}$ as in the bar legend at the bottom. Layer champions are in light brown, whereas the global champion $\hat{H}'$ is in orange.

Model	Experiment		Simulation	
	Wins	R^2	Wins	R^2
$\hat{S}_{y,z}\hat{A}_z$	9	0.8	1	0.26
$\hat{S}_y\hat{A}_{x,z}$	2	0.63		
$\hat{S}_{x,y,z}\hat{A}_z$	45	0.86	61	0.97
$\hat{S}_{x,y,z}\hat{A}_y$			1	-0.54
$\hat{S}_{x,y,z}\hat{A}_{x,y}$	3	0.81		
$\hat{S}_{x,y,z}\hat{A}_{y,z}$	14	0.83	10	0.96
$\hat{S}_{x,y,z}\hat{A}_{x,z}$	6	0.64	15	0.99
$\hat{S}_{x,y,z}\hat{A}_{x,y,z}$	2	0.72	5	0.97
$\hat{S}_{x,y,z}\hat{A}_{x,z}\hat{T}_{xz}$			1	0.68
$\hat{S}_{x,y,z}\hat{A}_{x,y,z}\hat{T}_{xz}$			5	0.77
$\hat{S}_y\hat{A}_{x,y,z}\hat{T}_{xy,xz,yz}$	2	0.31		
$\hat{S}_{x,y,z}\hat{A}_{x,y,z}\hat{T}_{xy,xz}$	4	0.67	1	0.32

Table 1.1: QMLA win rates and R^2 for models based on experimental data and simulations. We state the number of QMLA instances won by each model and the average R^2 for those instances as an indication of the predictive power of winning models.

the experimental case) shown in Fig. 1.5**(d)**. In particular, the most prominent models, $\{\hat{S}_{x,y,z}\hat{A}_z, \hat{S}_{x,y,z}\hat{A}_{y,z}, \hat{S}_{x,y,z}\hat{A}_{x,z}, \hat{S}_{y,z}\hat{A}_z\}$ are found collectively in 74% (87%) of instances on the experimental (simulated) data; the win rates and R^2 of all models (which won at least one instance) are reported in Table 1.1. It is noteworthy that even in the simulated case, the same models mislead QMLA: this suggests that the resultant physics from these models is substantially similar to that of the true model[7]. These models are defensible with respect to the descriptions of Section 1.2, since in each case they detect the interaction between the spin qubit and the environmental qubit, i.e. the hyperfine terms $\hat{A}_i$, especially $\hat{A}_z$ which occurs in 97% (99%) of champions. We discuss some physical insights from these results in Section 1.5.1.

The most frequently found model, $\hat{H}' = \hat{S}_{x,y,z}\hat{A}_z$, is found in 45% (61%) of instances: we show its attempt to reproduce the dynamics of Fig. 1.3 in Fig. 1.5**(e)**, showing excellent agreement with the raw data, with $R^2 = 0.82$. This serves as an essential sanity check: we can intuitively see that QMLA has distilled a model which captures at least *some* of the most important physical interactions the target NVC system is subject to; otherwise we would not see such clear overlap between the prediced and true dynamics.

Finally we display the model search as a in Fig. 1.5**(f)**, where models are represented on nodes on the graphs layers (equivalent to ET branches), and their parents are resident on the

---

6 Here we work backwards by setting the target model as that which QMLA deemed most appropriate for the available data. We posit that this choice is arbitrary and doesn't fundamentally change the discussion of this chapter, merely aiding in analysing the performance of the algorithm with respect to a concrete example.

7 Alternatively, that the same systematic error misdirects the search in both cases.

branch immediately above their own. Comparisons between models, $\hat{H}_i, \hat{H}_j$, are shown as edges between nodes on the graph, coloured by the strength of evidence of the outcome, the BF, B_{ij}. Each layer, μ, nominates their branch champion, $\hat{H}_{C(\mu)}$; the set of branch champions are consolidated to determine the global champion, $\hat{H}'_C$.

1.5.1   *Analysis*

Considering the runs summarised in Fig. 1.5, here we will present some furhter perspecitves. Fig. 1.6 first details all models considered in the 200 instances comprising the experimental and simulated QMLA runs, as well as the win rate of each model. This ES is designed to study a small subspace of the overall available space: only 40 unique models are constructed. We highlight a number of *credible* models which we deem especially valid approximations of the target system, i.e. which contain the most viable approximations.

Fig. 1.7 shows the reproduction of dynamics of the top four models from both simulated and experimental runs. We see that each model faithfully captures the essential dynamics arising from the respective target systems; this alone is insufficient to conclude that the true model has been identified, but serves as a valuable *sanity-check*, convincing us that the output of QMLA is at least a sensible approximation of $\hat{H}_0$, if not the absolutely true model.

The key insight promised by QMLA is to identfiy the interactions present in the studied system. In Fig. 1.8 we show the number of times each of the terms permitted (Eq. (2.3)) is included in the champion model; we also show the distribution of parameter estimates for those terms. From the simulated case, we see that those terms which are in $\hat{H}_0$, i.e. $\mathcal{T}_0$, are found in almost all instances; furthermore, while some terms are erroneoulsy found in $> 40\%$ of instances, they are found with less than a quarter of the frequency of the true terms, so these may be reasonably ruled out in post-processing the QMLA results. The inaccurate terms found most often are seen to have (almost) negligible parameters: in conjunction with domain expertise, users can determine whether the inclusion of these terms are meaningful or simply artefacts of slight overfitting. In the experimental run, on the other hand, we see a similar gulf in frequency between some terms. Namely, $\{\hat{S}_x, \hat{S}_y, \hat{S}_z, \hat{A}_z\}$ are found in 50+ more instances than all others: we therefore conclude that those terms contribute most strongly to the NVC. The parameters found for these terms are of the same order of magnitude as we would have predicted originally, but disagreee in the precise value. For example, the rotation about the y-axis, $\hat{S}_y$, has frequency 5.7MHz, roughly twice the predicted value of 2.7MHz.
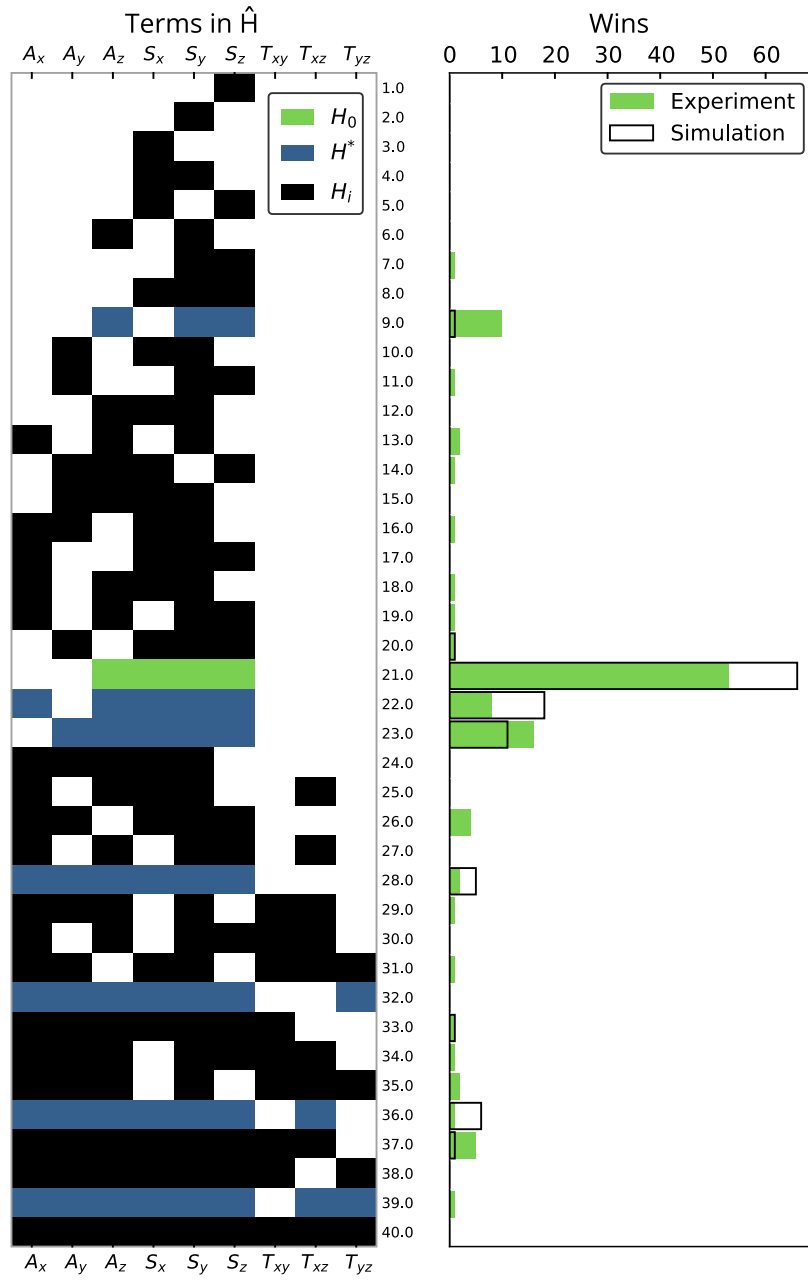
Figure 1.6: **Left**: map of the various Hamiltonian terms included in each of the possible 40 candidate models explored by QMLA during any of the 100 instances on either simulated or experimental data. The explicit form of each operator can be inferred from **??**. IDs of candidate models are on the vertical axis, and labels for the terms on the horizontal axis. The true model $\hat{H}_0$ for the simulated case is highlighted in green and a subset of credible models in blue, i.e. models which may reasonbaly be expected to describe the NVC from theoretical arguments. **Right**: wins for each of the candidate models as above out of 100 independent QMLA runs, reported as a histogram for cases adopting simulated data (empty bars) or the experimental dataset.
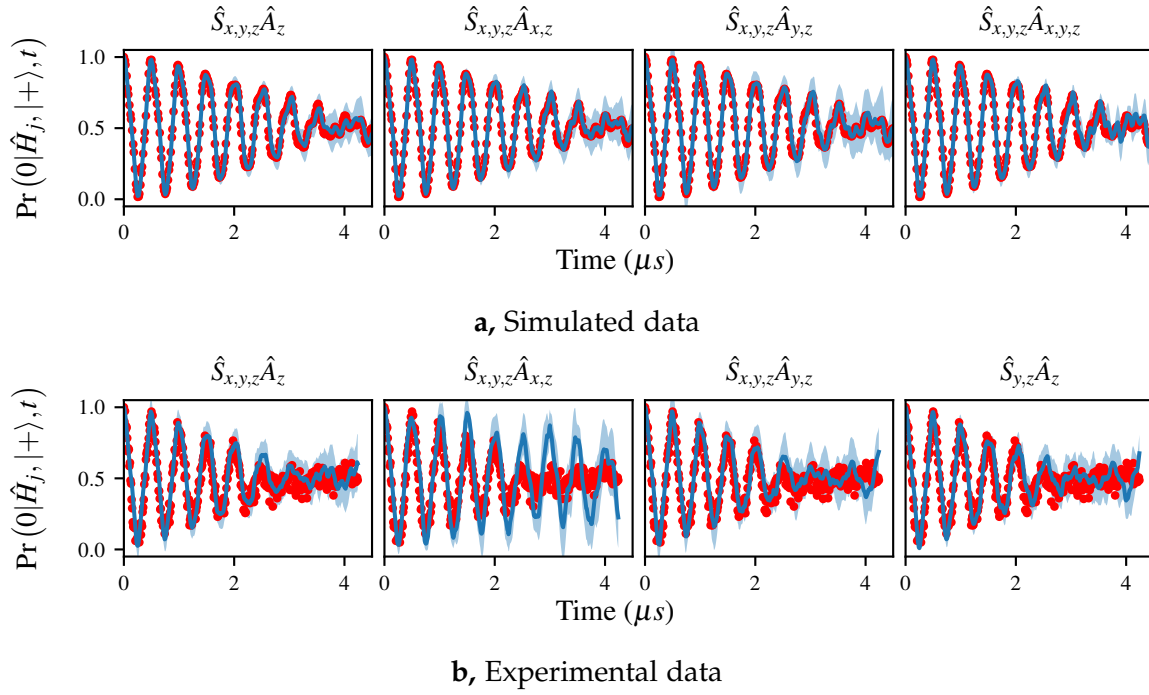
a, Simulated data

b, Experimental data

Figure 1.7: Dynamics reproduced by various QMLA champion models for simulated/experimental data. Expectation values are shown on y–axis with time on x–axis. Red dots give the true dynamics of $\hat{H}_0$, while the blue lines show the median reconstruction by $\hat{H}'$ from all the instance where that model was deemed $\hat{H}'$, with light blue showing the standard deviation of those likelihoods. $\hat{H}'$ is listed on top of each plot; the number of instances won by each model can be read from Table 1.1.
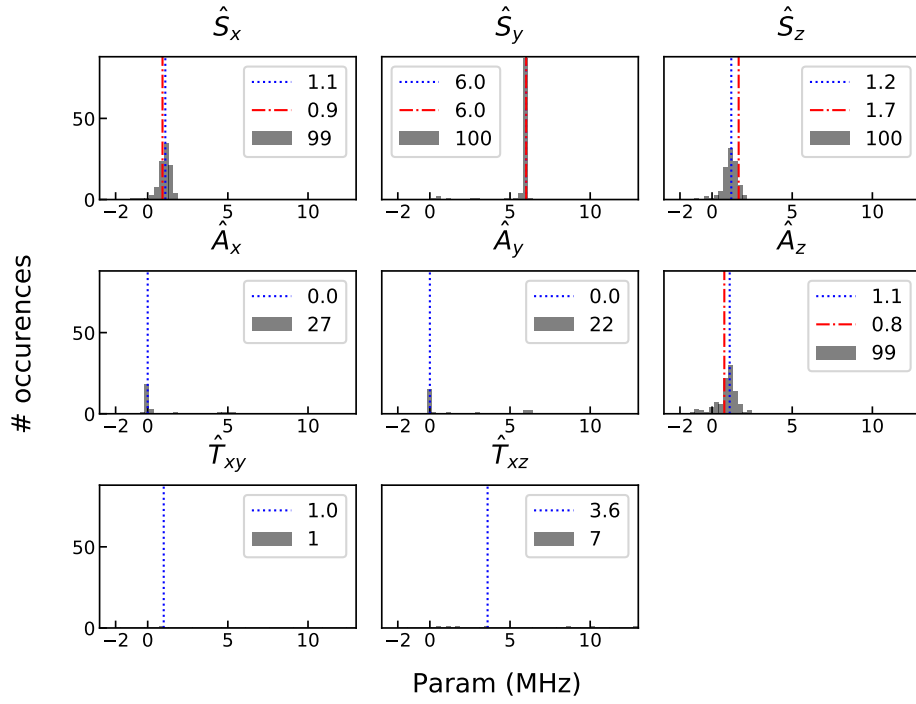
a, Simluated QMLA instances. Red dotted lines show the true parameters.
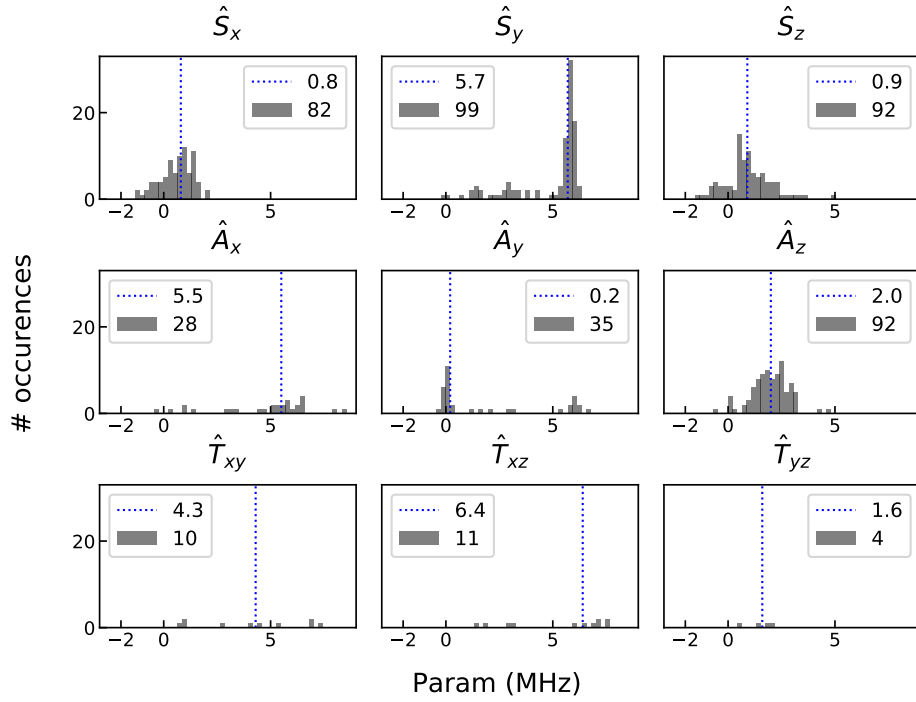
b, Experimental QMLA instances.

Figure 1.8: Histograms for parameters learned by QMLA champion models on (**a**) simulated and (**b**) experimental data. Blue dotted lines indicate the median for that parameter; grey blocks show the number of models which found the parameter to have that value and the number listed in the legend reports how many champion models contained that term.

2

EXTENSION TO MANY QUBITS

Chapter 1 concerned a two-qubit approximation of the short-time dynamics of an NVC. It is valid criticism of this analysis that the model space searched was reduced substantially from prior knowledge, and it therefore remains to test QMLA in a large model space, on physically meaningful data. In this chapter, we extend QMLA, to consider appoximations of NVC sytems using more qubits, representing several nuclear sites, which aim to capture the interactions between the target NVC and the environment. We will simulate the target system here, allowing us to make definite statements on the performance of QMLA, unlike the experimental data where we can not be sure of the dynamics' genreator.

2.1 TARGET SYSTEM

A more realistic model may be expected from consdiering the environment as a finite-size bath, consisting of n_s nuclear spins in addition to the NVC spin, i.e. the total number of qubits of such a model is $n_q = 1 + n_s$. Such effects can be highlighted by Hahn echo measurements, as in Fig. 1.2, except reversing the evoluting by $t' = t$ instead of $t' = 2t$ [13, 7], so our simulations will use this measurement scheme.

Since we are simulating the target system, we may choose the approximation we wish to invoke. We use the secular approximation, i.e. we assume the magnetic field is perfectly aligned along the z-axis [14]: recalling Eq. (1.1), the NVC spin qubit rotates only about the z-axis, and coupling between the electron and nuclear qubits are only via $\hat{S}_z \cdot \hat{A}_z^{\chi}$. We include the effect of the nuclear spins' rotations, which are much weaker. In total then, the set of nuclear spins, $\{\chi\}$, are mapped to n_s qubits:

$$\hat{H}_0 = \hat{S}_z + \sum_{j=2}^{n_q} \hat{S}_z \cdot \hat{A}_z^j + \sum_{w \in \{x,y,z\}} \sum_{j=2}^{n_q} \hat{I}_w^j. \tag{2.1}$$

For simplicity, we restate this in terms only of the Pauli matrices, where the first qubit refers to the NVC and the remaining qubits give the interactions and nuclear terms.

$$\hat{H}_0 = \hat{\sigma}_z^1 + \sum_{j=2}^{n_q} \hat{\sigma}_z^1 \hat{\sigma}_z^j + \sum_{w \in \{x,y,z\}} \sum_{j=2}^{n_q} \hat{\sigma}_w^j, \tag{2.2}$$

so in total, $\mathcal{T}_0$ has 1 term for the NVC qubit, n_s terms for hyperfine couplings and $3n_s$ terms for the nuclei: $|\mathcal{T}_0| = 1 + 4n_s$.
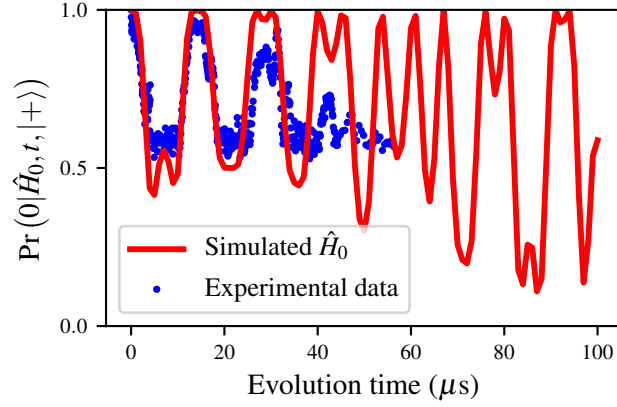
Figure 2.1: Long-time dynamics for nitrogen-vacancy centre, red, showing revivals, generated by $\hat{H}_0$ from Eq. (2.2). For comparison, experimentally generated dynamics are shown in blue.

We set the goal of QMLA as finding the approximation of Eq. (2.2), by allowing it to consider a wider set of terms. The permissible terms are then all spin rotation terms, as well as all nuclei rotation terms, and the coupling terms:

$$\mathcal{T} = \left\{ \begin{array}{c} \hat{S}_w = \hat{\sigma}_w^1, \\ \hat{I}_w^j = \hat{\sigma}_w^j, \\ \hat{S}_w \cdot \hat{A}_w = \hat{\sigma}_w^1 \hat{\sigma}_w^j \end{array} \right\} \tag{2.3}$$

for $w = \{x, y, z\}$ and $j \in \{2, ..., n_q'\}$. Importantly, in general $n_s' + 1 = n_q' \neq n_q$, i.e. QMLA can search a space of models with more or less spins, n_s', than are truly in $\hat{H}_0$. In total then, $|\mathcal{T}| = 3 + 3n_s' + 3n_s' = 3 + 6n_s'$.

We set the system parameters based on theoretical predictions, listed in Table 2.1.

Here our aim is to test QMLA, so the choice of n_s and n_s' are arbitrary; for the target system we use $n_s = 4$ proximal spins, so that, from Eq. (2.2), $|\mathcal{T}_0| = 13$, and we allow candidates to consider $n_s' = 5$, so $|\mathcal{T}| = 33$.

In summary, irrespective of the underlying physics we are simulating, here QMLA is aiming to identify the 13 terms truly present in Q, while searching the space of 33 permissible terms. Without imposing any restrictions on which combinations of terms are allowed, each term is simply either in $\hat{H}'$ or not, so can be thought of as binary variables: the total model space is therefore of size $2^{33} \approx 10^{10}$.

2.2 GENETIC ALGORITHM

GAs provide a robust and thoroughly tested paradigm for searching large candidate spaces; this is a natural framework through which we can explore such an unresetricted model space. We

Term	$\hat{t}$	Meaning	Parameter (Hz)	$\in \hat{H}_0$
$\hat{S}_x$	$\hat{\sigma}_x^1$	NVC rotation about x-axis	2×10^9	No
$\hat{S}_y$	$\hat{\sigma}_y^1$	NVC rotation about y-axis	2×10^9	No
$\hat{S}_z$	$\hat{\sigma}_z^1$	NVC rotation about z-axis	2×10^9	Yes
$\hat{S}_x \cdot \hat{A}_x^j$	$\hat{\sigma}_x^1 \hat{\sigma}_x^j$	Coupling b/w spin and j^{th} nuclear qubit about x-axis	0.2×10^6	No
$\hat{S}_y \cdot \hat{A}_y^j$	$\hat{\sigma}_y^1 \hat{\sigma}_y^j$	Coupling b/w spin and j^{th} nuclear qubit about y-axis	0.2×10^6	No
$\hat{S}_z \cdot \hat{A}_z^j$	$\hat{\sigma}_z^1 \hat{\sigma}_z^j$	Coupling b/w spin and j^{th} nuclear qubit about z-axis	0.2×10^6	Yes
$\hat{I}_x^j$	$\hat{\sigma}_x^j$	j^{th} nuclear spin rotation about x-axis	66×10^3	Yes
$\hat{I}_y^j$	$\hat{\sigma}_y^j$	j^{th} nuclear spin rotation about y-axis	66×10^3	Yes
$\hat{I}_z^j$	$\hat{\sigma}_z^j$	j^{th} nuclear spin rotation about z-axis	15×10^3	Yes

Table 2.1: Extended model NVC terms

have already extensively discussed the formalism of GAs in **??**, and specifically in the context of QMLA in **??**. Here we will use the same ES as described in **??**, i.e. where model generation is driven by a GA, and models are cast to chromosomes. In particular, candidate model's fitness will be computed from the residuals between their and the sytem's dynamics, described fully in **??**. This objective function (OF) relies on the definition of a validation dataset, $\mathcal{E}_v$, which we compose of tomographic probes and times generated uniformly up to $t_{max} = 100\mu s$, Fig. 2.2.

2.2.1 *Parameter learning*

Here, our primary goal is to validate QMLA's performance in a very large model space, with over 10^{10} valid candidates. Our focus on model generation, then, we do *not* train models individually: instead we assume access to a *perfect* parameter learning subroutine. That is, for each candidate considered, we simply assume knowledge of its parameters, $\vec{\alpha}$. This is a major caveat to the results of this chapter: no such perfect training scheme is known, so it remains to examine the detrimental effects of imprecisely finding $\vec{\alpha}' \approx \vec{\alpha}$. Moreover, while it is possible to extract information on the nuclear qubits from measuring only the NVC qubit, as in the Hahn echo measurements, it is uncertain whether any technique can simultaneously detect parameters of significantly varying orders of magnitude; For instance, some terms in Table 2.1 are $\mathcal{O}(\text{GHz})$, while others are $\mathcal{O}(\text{kHz})$; it is likely to prove difficult to discern the kHz parameters well, given that their contribution is equivalent to errors of order $\mathcal{O}(10^{-6})$ in the dominant GHz terms. Therefore we must caution that the results presented here, while demonstrating that QMLA *can* operate in large model spaces, are not immediately applicable to experimental systems, since
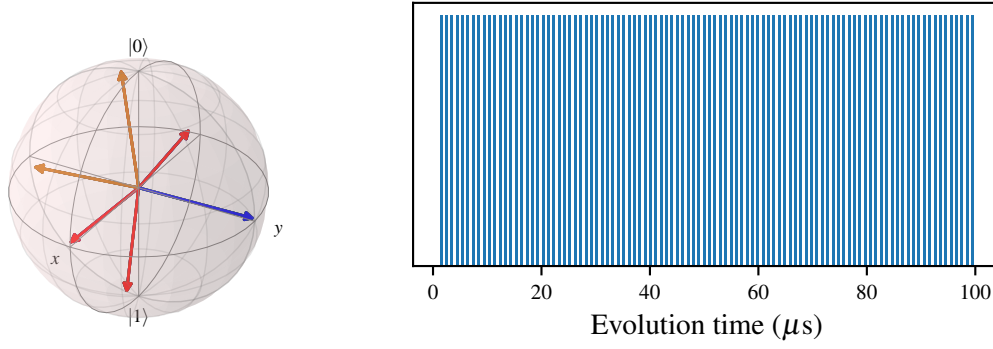
Figure 2.2: Evaluation dataset, $\mathcal{E}_v$, for nitrogen-vacancy centre genetic algorithm. **Left**, Probe state the NVC qubit is prepared in, on the Bloch sphere, **Right**, Time comb evaluated against, i.e. uniformly distributed times up to $t_{max} = 100\mu$s i.e. Ψ_v is close to the tomographic basis. are used for experiments in $\mathcal{E}_v$.

Qubit	$\hat{\sigma}_x^{(1,i)}$	$\hat{\sigma}_y^{(1,i)}$	$\hat{\sigma}_z^{(1,i)}$	$\hat{\sigma}_x^i$	$\hat{\sigma}_y^i$	$\hat{\sigma}_z^i$
1	-	-	-	0	0	100
2	5	11	97	97	99	97
3	10	9	94	96	94	94
4	7	12	94	94	97	95
5	9	12	11	6	8	5
6	7	9	9	7	5	8

Table 2.2: Percentage of instances for which each term is found by QMLA GA studying NVC system.

there are outstanding challenges in the assessment of individual candidates, which must be overcome before the technique outlined can realisitcally succeed.
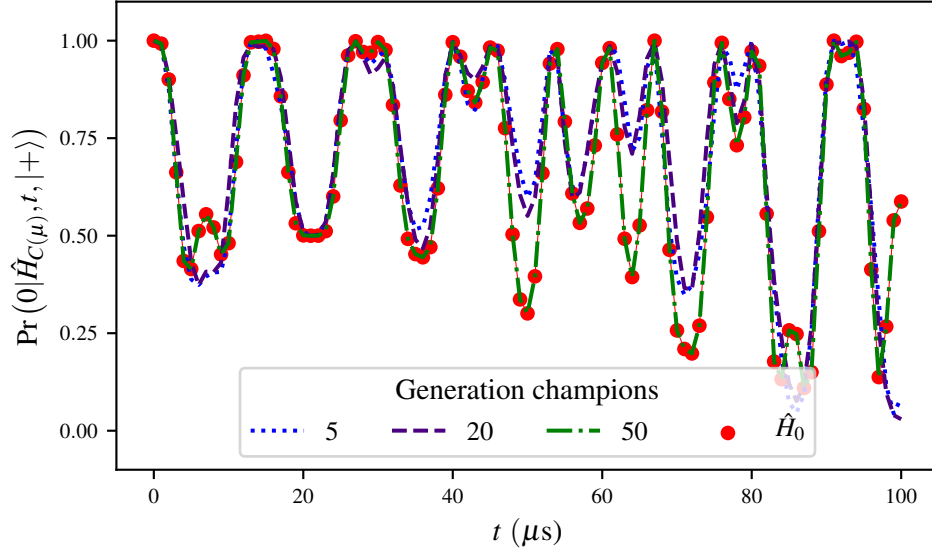
2.2.2   *Results*

Figure 2.3: Branch champions' dynamics. Each generation, μ, nominates a branch champion, $\hat{H}_{C(\mu)}$. Here, progressive generations' champions dynamics are shown against those of the target system, $\hat{H}_0$ (red).
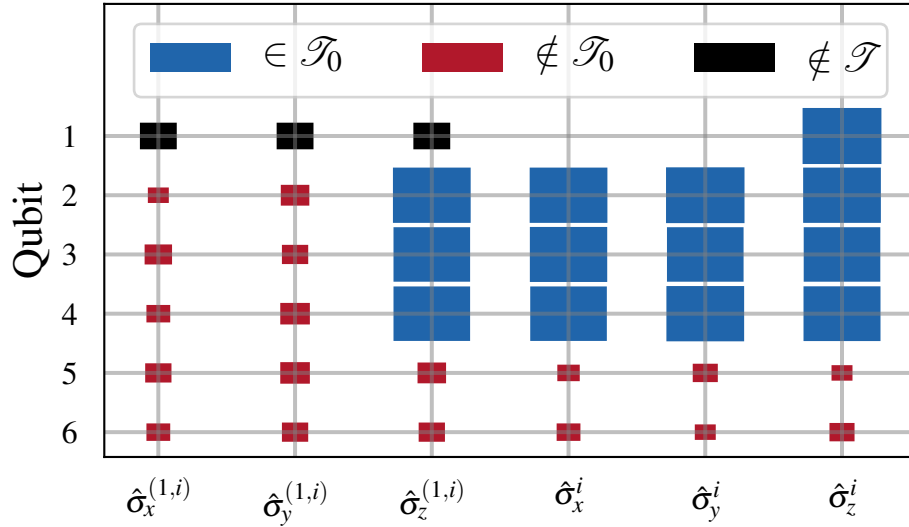

Figure 2.4: Hinton diagram of terms found for 4-qubit NVC model. Terms are either in the target model ($\in \mathcal{T}_0$, blue) or not ($\notin \mathcal{T}_0$, red), or else not considered ($\notin \mathcal{T}$, black). Terms acting solely on the first qubit are the NVC spin's rotation terms, $\hat{\sigma}_w^1$, while each nuclear site also has rotation terms $\hat{\sigma}_w^j$. Hyperfine terms, $\hat{\sigma}_w^{(1,j)}$, couple the NVC qubit with the jth nuclear spin. The precise rate at which each term is detected can be read from Table 2.2.

APPENDIX

A

Most of the figures presented in the main text are generated directly by the QMLA framework. Here we list the implementation details of each figure so they may be reproduced by ensuring the configuration in Table A.1 are set in the launch script. The default behaviour of QMLA is to generate a results folder uniquely identified by the date and time the run was launched, e.g. results can be found at the *results directory* qmla/Launch/Jan_01/12_34. Given the large number of plots available, ranging from high-level run perspective down to the training of individual models, we introduce a plot_level $\in \{1, ..., 6\}$ for each run of QMLA: higher plot_level informs QMLA to generate more plots.

Within the results directory, the outcome of the run's instances are stored, with analysis plots broadly grouped as

4. evaluation: plots of probes and times used as the evaluation dataset.

5. single_instance_plots: outcomes of an individual QMLA instance, grouped by the instance ID. Includes results of training of individual models (in model_training), as well as sub-directories for anlaysis at the branch level (in branches) and comparisons.

6. combined_datasets: pandas dataframes containing most of the data used during analysis of the run. Note that data on the individual model/instance level may be discarded so some minor analyses can not be performed offline.

7. exploration_strategy_plots plots specifically required by the ES at the run level.

8. champion_models: analysis of the models deemed champions by at least one instance in the run, e.g. average parameter estimation for a model which wins multiple instances.

9. performance: evaluation of the QMLA run, e.g. the win rate of each model and the number of times each term is found in champion models.

10. meta analysis of the algorithm' implementation, e.g. timing of jobs on each process in a cluster; generally users need not be concerned with these.

In order to produce the results presented in this thesis, the configurations listed in Table A.1 were input to the launch script. The launch scripts in the QMLA codebase consist of many configuration settings for running QMLA; only the lines in snippet in Listing A.1 need to be set according to altered to retrieve the corresponding figures. Note that the runtime of QMLA grows quite quickly with N_E, N_P (except for the AnalyticalLikelihood ES), especially for the entire QMLA algorithm; running QHL is feasible on a personal computer in < 30 minutes for $N_e = 1000; N_p = 3000$.

```bash
#!/bin/bash
```

```
##############
# QMLA run configuration
##############
num_instances=1
run_qhl=1 # perform QHL on known (true) model
run_qhl_mulit_model=0 # perform QHL for defined list of models.
exp=200 # number of experiments
prt=1000 # number of particles

##############
# QMLA settings
##############
plot_level=6
debug_mode=0

##############
# Choose an exploration strategy
##############

exploration_strategy='AnalyticalLikelihood'
```

Listing A.1: "QMLA Launch scipt"

Figure	Exploration Strategy	Algorithm	N_E	N_P	Data
??	AnalyticalLikelihood	QHL	500	2000	Nov_16/14_28
??	DemoIsing	QHL	500	5000	Nov_18/13_56
??	DemoIsing	QHL	1000	5000	Nov_18/13_56
??	DemoIsing	QHL	1000	5000	Nov_18/13_56
??	IsingLatticeSet	QMLA	1000	4000	Nov_19/12_04
	IsingLatticeSet	QMLA	1000	4000	Sep_30/22_40
??	HeisenbergLatticeSet	QMLA	1000	4000	Oct_22/20_45
	FermiHubbardLatticeSet	QMLA	1000	4000	Oct_02/00_09
	DemoBayesFactorsByFscore	QMLA	500	2500	Dec_09/12_29
??	DemoFractionalResourcesBayesFactorsByFscore	QMLA	500	2500	Dec_09/12_29
	DemoBayesFactorsByFscore	QMLA	1000	5000	Dec_09/12_29
	DemoBayesFactorsByFscoreEloGraphs	QMLA	500	2500	Dec_09/12_29

Table A.1: Implementation details for figures used in the main text.

B

EXAMPLE EXPLORATION STRATEGY RUN

A complete example of how to run the ;sqmla framework, including how to implement a custom ES, and generate/interpret analysis, is given.

BIBLIOGRAPHY

[1] Marcus W Doherty, Neil B Manson, Paul Delaney, Fedor Jelezko, Jörg Wrachtrup, and Lloyd CL Hollenberg. The nitrogen-vacancy colour centre in diamond. *Physics Reports*, 528(1):1–45, 2013.

[2] Gordon Davies and MF Hamer. Optical studies of the 1.945 ev vibronic band in diamond. *Proceedings of the Royal Society of London. A. Mathematical and Physical Sciences*, 348(1653):285–298, 1976.

[3] J Meijer, B Burchard, M Domhan, C Wittmann, Torsten Gaebel, I Popa, F Jelezko, and J Wrachtrup. Generation of single color centers by focused nitrogen implantation. *Applied Physics Letters*, 87(26):261909, 2005.

[4] AM Edmonds, UFS D'Haenens-Johansson, RJ Cruddace, ME Newton, K-MC Fu, C Santori, RG Beausoleil, DJ Twitchen, and ML Markham. Production of oriented nitrogen-vacancy color centers in synthetic diamond. *Physical Review B*, 86(3):035201, 2012.

[5] A Lenef and SC Rand. Electronic structure of the n-v center in diamond: Theory. *Physical Review B*, 53(20):13441, 1996.

[6] Benjamin Smeltzer, Lilian Childress, and Adam Gali. 13c hyperfine interactions in the nitrogen-vacancy centre in diamond. *New Journal of Physics*, 13(2):025021, 2011.

[7] Heinz-Peter Breuer, Francesco Petruccione, et al. *The theory of open quantum systems*. Oxford University Press on Demand, 2002.

[8] Antonio A. Gentile, Brian Flynn, Sebastian Knauer, Nathan Wiebe, Stefano Paesani, Christopher E. Granade, John G. Rarity, Raffaele Santagati, and Anthony Laing. Learning models of quantum systems from experiments, 2020.

[9] MS Blok, Cristian Bonato, ML Markham, DJ Twitchen, VV Dobrovitski, and R Hanson. Manipulating a qubit through the backaction of sequential partial measurements and real-time feedback. *Nature Physics*, 10(3):189–193, 2014.

[10] Adam Gali, Maria Fyta, and Efthimios Kaxiras. Ab initio supercell calculations on nitrogen-vacancy center in diamond: Electronic structure and hyperfine tensors. *Physical Review B*, 77(15):155206, 2008.

[11] MV Gurudev Dutt, L Childress, L Jiang, E Togan, J Maze, F Jelezko, AS Zibrov, PR Hemmer, and MD Lukin. Quantum register based on individual electronic and nuclear spin qubits in diamond. *Science*, 316(5829):1312–1316, 2007.

[12] P-Y Hou, L He, F Wang, X-Z Huang, W-G Zhang, X-L Ouyang, X Wang, W-Q Lian, X-Y Chang, and L-M Duan. Experimental hamiltonian learning of an 11-qubit solid-state quantum spin register. *Chinese Physics Letters*, 36(10):100303, 2019.

[13] L Childress, MV Gurudev Dutt, JM Taylor, AS Zibrov, F Jelezko, J Wrachtrup, PR Hemmer, and MD Lukin. Coherent dynamics of coupled electron and nuclear spin qubits in diamond. *Science*, 314(5797):281–285, 2006.

[14] L G Rowan, EL Hahn, and WB Mims. Electron-spin-echo envelope modulation. *Physical Review*, 137(1A):A61, 1965.

[15] Forrest T Charnock and TA Kennedy. Combined optical and microwave approach for performing quantum spin operations on the nitrogen-vacancy center in diamond. *Physical Review B*, 64(4):041201, 2001.

[16] Antonio Andreas Gentile. *Operating practical quantum devices in the pre-threshold regime*. PhD thesis, University of Bristol, 2020.

[17] Stuart Russell and Peter Norvig. Artificial intelligence: a modern approach. 2002.

[18] David A Broadway, Jean-Philippe Tetienne, Alastair Stacey, James DA Wood, David A Simpson, Liam T Hall, and Lloyd CL Hollenberg. Quantum probe hyperpolarisation of molecular nuclear spins. *Nature communications*, 9(1):1–8, 2018.